3D Measurement of Complex Textured Objects Based on Bidirectional Fringe Projection

Yuchong Chen, Jian Yu*, Shaoyan Gai, Zeyu Cai, Feipeng Da*

School of Automation, Southeast University
MoE Key Laboratory of Measurement and Control of Complex Systems of Engineering, Southeast University
{230228469, yujian, 101011375, zeyucai, dafp}@seu.edu.cn,

Abstract

In structured light systems, the accuracy of measurement notably diminishes when assessing complex texture objects, especially encountering boundaries between various colors. To address this challenge, this paper meticulously analyzes and establishes an error model, elaborating the correlation between phase errors and the gradients of phase and grayscale. Based on this analysis, a novel high-precision method is proposed for measuring complex texture objects via bidirectional fringe projection. This approach firstly leverages horizontal and vertical fringe projections to derive bidirectional phase information and calculates the angles between the tangent of the texture edges and the phase gradient. Subsequently, a refined temporal phase correction algorithm is formulated based on the epipolar matching algorithm and the devised error model, effectively reducing errors caused by complex textures. Ultimately, corrected point clouds are calculated based on bidirectional phases, and the obtained point clouds are merged to further diminish phase errors. Comparison experiments indicate that this method can reduce Mean Absolute Error (MAE) and Root Mean Square Error (RMSE) by 65.74% and 67.75%, respectively. Compared to existing methods, it improves performance by 27.29% and 33.74%, respectively, demonstrating superior performance.

Introduction

Recovering dense 3D shapes of objects from 2D images is a fundamental artificial intelligence problem, with many research results achieved (Zhang and Yau 2006; Zhang et al. 2019; Khan, Shirazi, and Kim 2018). The point cloud obtained by 3D reconstruction can be used in numerous fields, such as object detection, object tracking, and 3D shape features learning (Yan et al. 2017; Koh et al. 2022; Li and Cheng 2022). Therefore, optimizing point clouds and reconstruction algorithms is also a meaningful research direction.

Fringe projection profilometry (FPP) holds a dominant position among various reconstruction algorithms due to its low cost, strong robustness, and high spatial resolution (Su and Zhang 2010; Geng 2011; Quan, Tay, and Chen 2007). Furthermore, the rapid development of digital light processing (DLP) techniques promotes the research of FPP. Three-dimensional measurement technology based on structured light assumes that each camera pixel exclusively captures light emanating from one projector pixel. However, this assumption often fails to hold in many actual measurement situations, such as inter-reflection, subsurface scattering, volumetric scattering, camera defocusing and so on (Nayar et al. 2006; Kobayashi et al. 2015; Sun et al. 2022). These situations are generally referred to multi-path issues that a camera pixel sees light emanating from multiple projector pixels (Zhang, Lau, and Yu 2019; Zhang, Lau, and Wipf 2021).

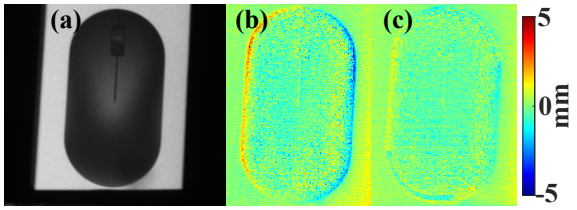

Figure 1: A flat plate is measured using FPP. (a) A flat plate adorned with a mouse pattern; (b) Point cloud error caused by defocusing of complex texture; (c) Point cloud error corrected by the proposed method.

Among these situations, lens defocusing is inevitable for every camera, which severely impair the performance of three-dimensional optical measurement techniques. Due to camera defocusing, each camera pixel essentially captures the convolution of the point spread function (PSF) with the intensity of light reflected from points in a specific region on the object. For objects without texture, where the surface reflectivity can be considered uniform, the impact of defocusing is minimal, allowing FPP to attain exceptional reconstruction accuracy. Conversely, for objects with complex textures, especially around edges where surface colors change, the convolution between the disparate reflectivities of surface points and PSF leads to cross-contamination in grayscale of fringe patterns. In the phase data, this manifests as the phase of contamination points being biased towards regions with higher reflectivity, thereby adversely affecting the accuracy of the final reconstruction (Yao et al. 2024). An example of these objects is illustrated in Fig. 1, where the errors in the point cloud caused by complex textures are distinctly evident. Currently, many researchers have proposed

*Corresponding author.

various error analysis and phase compensation algorithms. Broadly, these algorithms are categorized into two groups: one involves estimating the PSF distribution of the camera, while the other employs error compensation via the Single-Pixel Imaging Method (SIM). However, the former relies on the accurate neighborhood information of pixels to correct phase errors, while the latter is characterized by lower computational efficiency.

Based on our previous research on multi-path issues, we further introduce a temporal phase correction algorithm, termed the Epipolar Line Phase Correction and Point Cloud Fusion (ELPC-PCF) algorithm. This algorithm effectively corrects errors induced by complex textures in FPP, while obviating the need for additional equipments and maintaining high stability. Through a series of comparison experiments, we have validated the accuracy of the proposed algorithm. As illustrated in Fig. 1(c), this method significantly reduces point cloud errors caused by complex textures.

Our contributions are summarized as follows:

- We conducted an in-depth analysis of the phase error model within areas of abrupt reflectivity transition when subjected to camera defocusing. This investigation revealed an obvious correlation between phase errors, phase gradients, and gray-scale gradients.
- Based on this proposed error model, we projected both horizontal and vertical fringe patterns to capture bidirectional phase information. A temporal phase error correction algorithm ELPC was developed, grounded on the epipolar matching algorithm and the proposed error model. Unlike traditional algorithms, ELPC provides sufficient constraints to directly correct phase errors without the need for complex parameter calibration.
- Finally, we synthesized and refined point clouds using bidirectional phase information, significantly minimizing phase errors. Comparison experiments confirmed the efficacy of our method, showcasing a reduction in MAE and RMSE by 65.74% and 67.75%, respectively.

Related Work

Although numerous deblurring methods exist at present (Wu et al. 2016; Hosseini and Plataniotis 2019; Xu and Jia 2010; Biggs and Andrews 1997), none can achieve absolute focus, rendering the phase errors caused by complex textures unavoidable. By estimating the PSF distribution, phase pattern can be categorized into accurate and erroneous regions. Rao et al., building on the algorithm outlined in literature (Joshi, Szeliski, and Kriegman 2008), derived the PSF distribution and subsequently developed an two-dimensional error model (Rao and Da 2018). Utilizing this foundation, they calculated phase compensation values by harnessing the phase and phase gradients from neighboring accurate regions. Hu et al. further simplified the two-dimensional phase error model to a one-dimensional model by imposing ideal constraints (Hu et al. 2023). They introduced a method for estimating parameters under both degenerate and nondegenerate reflectivity discontinuities, facilitating phase correction. Wu et al. estimated the PSF by fitting a Gaussian curve and then performed deconvolution on the captured patterns using the obtained PSF (Wu et al. 2020). Yue et al. utilized the intensity and phase values of adjacent accurate regions to derive an error expression for the erroneous regions, thereby achieving phase optimization (Yue et al. 2019). Nonetheless, the efficacy of these method hinges on the precision of PSF estimation, which may falter in environments with rapid reflectivity transitions, diminishing the accuracy of error compensation. Additionally, Blanchard et al. proposed a method for correcting point cloud errors based on Gaussian curve fitting, but this method is limited to planar objects (Blanchard and Zhang 2022).

Diverging from PSF distribution estimation (Wu et al. 2019), SIM compensates phase errors through reconstructing scene reflectivity. Traditional SIM modulates images using a spatial light modulator and records the total reflected light intensity with a single-pixel detector. Through multiple measurements, the reflectivity of the scene is then deduced (Edgar, Gibson, and Padgett 2019; Zhang et al. 2017; Qiu et al. 2020). To reduce hardware requirements, Parallel Single-Pixel Imaging (PSI) was developed, necessitating merely a projector and a camera. This innovation leverages the projector to project requisite patterns, considering each camera pixel as an independent single-pixel detector for reflectivity reconstruction (Ma et al. 2021; Wang et al. 2021; Jiang et al. 2021; Lyu et al. 2024). However, such methods still require capturing thousands of frames and extensive data computation. Consequently, Lyu et al. introduced FPP for coarse pixel matching, thereby reducing measurement time to 8% of that required by traditional SIM (Lyu et al. 2023). This approach is predicated on the assumption that the PSF of camera follows a Gaussian distribution and that the defocusing is minor.

Error Analysis and Error Model

This section initiates with an analysis of phase errors in objects with complex textures, subsequently establishing a reliable error model. It reveals a correlation between phase errors and both phase and grayscale gradients. The details of the formula derivation can be found in the **Appendix**.

Fig. 2(a) illustrates a typical FPP system, consisting of a camera and a projector. During the measurement process, the DLP projects a series of fringe patterns onto the measured object. Subsequently, the camera captures the fringe patterns modulated by the object shape. Finally, the fringe patterns are decoded and unwrapped to recover the absolute phase. Based on the triangulation relationship between the camera and projector, this absolute phase is reconstructed

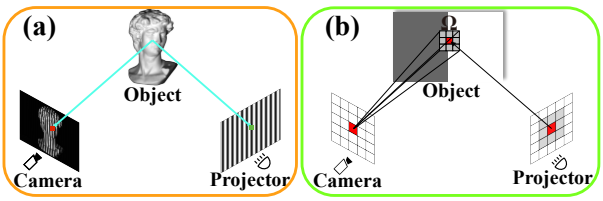

Figure 2: (a) FPP system schematic; (b) Schematic of complex texture object measurement under camera defocusing.

into a 3D point cloud of the measured object. The captured sinusoidal fringe patterns can be expressed as:

$$I_n^c(u_c, v_c) = r(u_c, v_c)\{I_1 + I_2 \cos[\phi(u_c, v_c) + \delta_n]\} + I_0, \quad n = 1, 2, \ldots, N, \tag{1}$$

where, I_n^c denotes the n_{th} phase-shifting pattern; (u_c, v_c) denotes the pixel coordinate on the imaging plane of the camera; r denotes the reflectivity of object surface; I_1 and I_2 denotes the average intensity and intensity modulation, respectively; I_0 denotes the ambient intensity; ϕ denotes the unwrapped phase; $\delta_n = 2\pi(n-1)/N$ denotes the amount of phase shift; and N is the total number of phase-shifting patterns.

As depicted in Fig. 2(b), when the camera is defocused, a pixel on the imaging plane of camera no longer merely captures light from a single pixel on the projector. Instead, it receives reflected light intensities from multiple points within the range of the PSF on the object surface. At this point the captured fringe patterns can be modified as:

$$\begin{aligned} I_n^g(u_c, v_c) &= G(x, y) * I_n^c(u_c, v_c) \\ &= \iint_\Omega G(x, y) I_n^c(u_c + x, v_c + y)\, \mathrm{d}x\mathrm{d}y, \end{aligned} \tag{2}$$

where, $*$ denotes convolution operation; Ω denotes the defocusing window; and (x, y) denotes a location index in the window. $G(x, y)$ represents the PSF of the camera, which can be described by a Gaussian function with a standard deviation of σ (Zuo et al. 2018), as shown in Eq. (3). For brevity in subsequent equations, $G(x, y)$ will be abbreviated as G_{xy}.

$$G(x, y) = \frac{1}{2\pi\sigma^2} e^{-\frac{x^2+y^2}{2\sigma^2}}. \tag{3}$$

The coordinate systems of the camera and the projector converge on the object surface, allowing for direct analysis of errors from the perspective of projector. As depicted in Fig. 3(a), a new coordinate system xoy is established with the origin at (u_c, v_c). The pixel coordinates of the projector are denoted as (u_p, v_p). The green line represents the texture edge where the reflectivity changes abruptly. The phase at the origin (u_c, v_c) after defocusing can be expressed as (Rao and Da 2018):

$$\begin{aligned} \phi'(u_c, v_c) &= \arctan \frac{-\sum_{n=1}^{N} \sin(\delta_n) I_n^g(u_c, v_c)}{\sum_{n=1}^{N} \cos(\delta_n) I_n^g(u_c, v_c)} \\ &= \arctan \frac{\iint_\Omega G_{xy} r(x, y) \sin[\phi(x, y)]\, \mathrm{d}x\mathrm{d}y}{\iint_\Omega G_{xy} r(x, y) \cos[\phi(x, y)]\, \mathrm{d}x\mathrm{d}y}. \end{aligned} \tag{4}$$

Assuming the projected fringes vary uniformly along the x axis with a period t, it follows that $\phi(x, y) = 2\pi x/t + \phi(u_c, v_c)$. The angle between this direction and the texture edge is α in the counterclockwise direction. In xoy coordinate system, the boundary of the defocus region Ω is considered as being at infinity. It should be noted that the actual range of camera defocus is very small, hence the phase change within region Ω is minimal, i.e., $2\pi x/t \to 0$. Based on this, the difference between ϕ' and the ground truth of ϕ is (Rao and Da 2018):

$$\begin{aligned} \triangle\phi(u_c, v_c) &= \arctan \frac{\iint_\Omega G_{xy} r(x, y) \sin(2\pi x/t)\, \mathrm{d}x\mathrm{d}y}{\iint_\Omega G_{xy} r(x, y) \cos(2\pi x/t)\, \mathrm{d}x\mathrm{d}y} \\ &\approx \arctan \frac{\iint_\Omega G_{xy} r(x, y) 2\pi x\, \mathrm{d}x\mathrm{d}y}{\iint_\Omega G_{xy} r(x, y) t\, \mathrm{d}x\mathrm{d}y}. \end{aligned} \tag{5}$$

Consequently, the corresponding projector coordinate error can be obtained:

$$\begin{aligned} \triangle u_p &= \frac{\triangle\phi(u_c, v_c) t}{2\pi} \approx \frac{\iint_\Omega G_{xy} r(x, y) x\, \mathrm{d}x\mathrm{d}y}{\iint_\Omega G_{xy} r(x, y)\, \mathrm{d}x\mathrm{d}y} \\ &= \frac{\iint_{\Omega_1} G_{xy} r_1 x\, \mathrm{d}x\mathrm{d}y + \iint_{\Omega_2} G_{xy} r_2 x\, \mathrm{d}x\mathrm{d}y}{\iint_{\Omega_1} G_{xy} r_1\, \mathrm{d}x\mathrm{d}y + \iint_{\Omega_2} G_{xy} r_2\, \mathrm{d}x\mathrm{d}y}, \end{aligned} \tag{6}$$

where, r_1 represents the reflectivity of the object at region Ω_1, and r_2 represents the reflectivity of the object at region Ω_2. By deriving the four parts of this expression separately, the following four equations can be obtained:

$$\iint_{\Omega_1} G_{xy} r_1 x\, \mathrm{d}x\mathrm{d}y = \frac{r_1 \sigma \sin\alpha}{\sqrt{2\pi}}, \tag{7}$$

$$\iint_{\Omega_1} G_{xy} r_1\, \mathrm{d}x\mathrm{d}y = \frac{r_1}{2}, \tag{8}$$

$$\iint_{\Omega_2} G_{xy} r_2 x\, \mathrm{d}x\mathrm{d}y = -\frac{r_2 \sigma \sin\alpha}{\sqrt{2\pi}}, \tag{9}$$

$$\iint_{\Omega_2} G_{xy} r_2\, \mathrm{d}x\mathrm{d}y = \frac{r_2}{2}. \tag{10}$$

By substituting Eqs. (7-10) into Eq. (6), the specific form of the coordinate error can be obtained:

$$\triangle u_p = \sqrt{\frac{2}{\pi}} \frac{r_1 - r_2}{r_1 + r_2} \sigma \sin\alpha. \tag{11}$$

However, Fig. 3(a) represents the ideal case for complex textures. In reality, the texture edge does not exactly pass through the center point of the defocus region, as shown by the green solid line in Fig. 3(b). Under this circumstance, the reflected light intensity from the object within region Ω_3 differs from the ideal situation depicted in Fig. 3(a). Therefore, the coordinate error becomes:

$$\triangle u_p = \frac{\iint_\Omega G_{xy} r(x, y) x\, \mathrm{d}x\mathrm{d}y + \iint_{\Omega_3} G_{xy} (r_1 - r_2) x\, \mathrm{d}x\mathrm{d}y}{\iint_\Omega G_{xy} r(x, y)\, \mathrm{d}x\mathrm{d}y + \iint_{\Omega_3} G_{xy} (r_1 - r_2)\, \mathrm{d}x\mathrm{d}y}. \tag{12}$$

From Fig. 3(b), the following parameter relationships can be derived:

$$\begin{cases} \beta = \frac{\cos\alpha}{\sin\alpha} \\ d = \mu \sin\alpha \end{cases}. \tag{13}$$

$$\iint_{\Omega_3} G_{xy} (r_1 - r_2) x\, \mathrm{d}x\mathrm{d}y = \frac{(e^{-\frac{d^2}{2\sigma^2}} - 1)(r_1 - r_2)\sigma \sin\alpha}{\sqrt{2\pi}}. \tag{14}$$

By rotating xoy coordinate system of Fig. 3(b) around the center point o, Fig. 3(c) is obtained. Based on the properties of the Gaussian function, the following equation can be derived:

$$\begin{aligned} &\iint_{\Omega_3} G_{xy} (r_1 - r_2)\, \mathrm{d}x\mathrm{d}y = \iint_{\Omega_4} G_{xy} (r_1 - r_2)\, \mathrm{d}x\mathrm{d}y \\ &= \frac{(r_1 - r_2)}{2} erf(d/\sqrt{2}\sigma). \end{aligned} \tag{15}$$

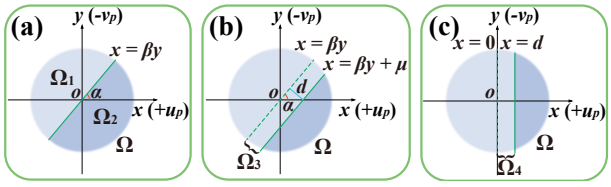

Figure 3: (a) Ideal case for complex textures; (b) Non-ideal case for complex textures; (c) Non-ideal case for complex textures after rotating the coordinate system.

Eqs. (14) and (15) represent the contributions from region Ω_3. Substituting these into Eq. (12), the specific formula for coordinate error under general conditions can be derived:

$$\triangle u_p = \sqrt{\frac{2}{\pi}} \frac{r_1 - r_2}{r_1 + r_2 + (r_1 - r_2) erf(d/\sqrt{2}\sigma)} \sigma e^{-\frac{d^2}{2\sigma^2}} \sin\alpha. \tag{16}$$

It can be observed that this error is independent of the fringe period t. Based on this formula, it is possible to plot the variation of errors under different conditions, as illustrated in Fig. 4(a). The parameters are set as follows: $\sigma = 1$, $r_1 = 0.8$, $r_2 = 0.2$; the top view of Fig. 4(a) is shown in Fig. 4(b). Notably, consistent with Fig. 3(c), $d > 0$ indicates that the imaging center point o is located in the high reflectivity region, while $d < 0$ indicates it is located in the low reflectivity region. Fig. 4(c) displays the error variation curves as a function of the angle α for different values of d. Fig. 4 reveals deeper characteristics of the error caused by abrupt changes in reflectivity:

1. It is evident that when the texture edge is perpendicular to the phase gradient, i.e., $\alpha = \pm\pi/2$, the error is maximized, whereas there is no error when they are parallel.
2. When α is fixed, the pixel located at the ideal position, i.e., $d = 0$, is not the pixel with the greatest error. Conversely, as shown in Fig. 4(b), the error is maximized when $d < 0$, i.e., when the imaging center point o is located in the low reflectivity region. This indicates that, when using surrounding pixels to assist in phase correction, priority should be given to pixels in high reflectivity regions, excluding those in low reflectivity regions.
3. For any value of d, the error is a trigonometric function of the angle α, exhibiting clear regularity, which is crucial for correcting this error.

The above derivation is based on the assumption that the phase changes uniformly along the x ($+u_p$) axis, which implies that the projector is projecting horizontal fringes. When the projector projects vertical fringes, the direction of fringe variation becomes $-y$ ($+v_p$), and the angle α changes to $\alpha + \pi/2$. Consequently, the error formula for the projector coordinate (u_p, v_p) can be derived as Eqs. (17) and (18):

$$\begin{cases} \triangle u_p = k \sin\alpha \\ \triangle v_p = k \cos\alpha \end{cases}, \tag{17}$$

$$k = \sqrt{\frac{2}{\pi}} \frac{r_1 - r_2}{r_1 + r_2 + (r_1 - r_2) erf(d/\sqrt{2}\sigma)} \sigma e^{-\frac{d^2}{2\sigma^2}}. \tag{18}$$

The above constitutes the error model of projector coordinate for regions with abrupt changes in reflectivity proposed in this paper. Given the small range of defocusing, it typically does not affect phase unwrapping; hence, $\triangle u_p$ and $\triangle v_p$ can be considered as the final coordinate error.

Correction Method Based on Bidirectional Phase

This section details the construction and implementation of a phase error correction method, which is based on the epipolar matching algorithm and the proposed error model. Furthermore, by leveraging bidirectional phase information, the precision of the algorithm is significantly enhanced.

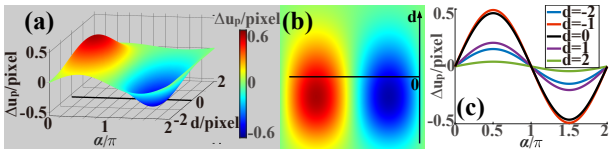

Figure 4: (a) Error caused by complex textures; (b) Top view of the error; (c) Cross-sectional view of the error.

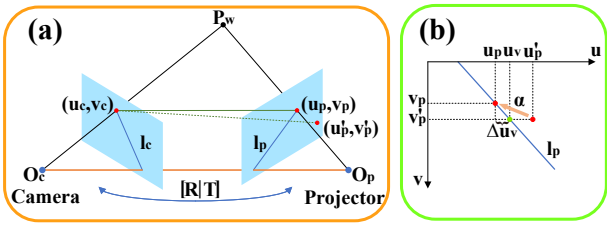

Figure 5: (a) Schematic diagram of epipolar line matching; (b) Schematic diagram of error correction.

Epipolar Compensation Method

Building upon Eq. (17), we propose a novel temporal compensation strategy that projects horizontal and vertical phase-shifting patterns to capture bidirectional phase information. Given that the angle α at texture edges can be straightforwardly extracted using operators like Sobel in actual measurements, it is considered known. However, Eq. (17) comprises three unknowns ($\triangle u_p$, $\triangle v_p$ and k) with only two equations, making it impossible to solve accurately. To address this, this paper introduces an additional constraint through the epipolar matching algorithm, based on the bidirectional phase information. As shown in Fig. 5(a), there exists an epipolar geometry constraint between the camera and the projector. The optical centers of the camera O_c and the projector O_p, along with a point P_w in three-dimensional space, form an epipolar plane. This plane intersects the imaging planes of both the camera and the projector at epipolar lines l_c and l_p, respectively. The projector pixel (u_p, v_p) projects to P_w, which is then captured by the camera and imaged at camera pixel (u_c, v_c). Ideally, (u_p, v_p) and (u_c, v_c) are precisely situated on the epipolar lines l_c and l_p, respectively. The epipolar line l_p can be expressed as:

$$\begin{aligned} l_p &= F \times [u_c, v_c, 1]^T = [a, b, c]^T \\ F &= K_p^{-T} \times (T \times R) \times K_c^{-1} \end{aligned}, \tag{19}$$

where, F denotes the fundamental matrix; K_p and K_c represent the intrinsic parameters of the projector and camera, respectively; a, b, and c are the coefficients of the epipolar line l_p; and R and T respectively signify the rotation and translation matrices that describe the transformation from the camera coordinate system to the projector coordinate system. The epipolar line l_p is finally represented as:

$$a u_p + b v_p + c = 0. \tag{20}$$

Fig. 5(b) illustrates the image coordinate system of the projector, where superscript $'$ denotes the coordinate con-

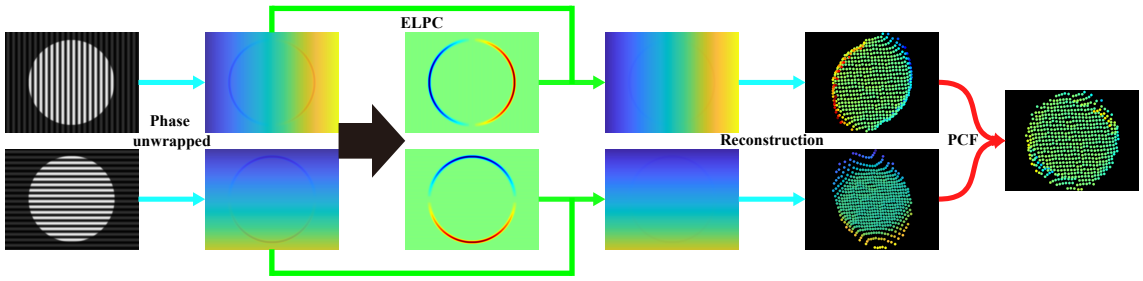

Figure 6: The flowchart of ELPC-RPF.

taining errors. Owing to the camera defocusing and the complex textures, phase error arise at the correct projector pixel (u_p, v_p) associated with the camera pixels (u_c, v_c). Consequently, this leads to erroneous positioning, causing a deviation from the epipolar line to (u'_p, v'_p). After system calibration, the known intrinsic and extrinsic parameters for both the camera and projector allow the coefficients of the epipolar line function to be calculated directly using Eq. (19). Thus, Eq. (20) supplements Eq. (17) with an additional usable equation, fulfilling the prerequisites for solution derivation. After organizing, the linear system of equations can be obtained as follows:

$$\begin{bmatrix} 1 & 0 & \sin\alpha \\ 0 & 1 & \cos\alpha \\ a & b & 0 \end{bmatrix} \begin{bmatrix} u_p \\ v_p \\ k \end{bmatrix} = \begin{bmatrix} u'_p \\ v'_p \\ -c \end{bmatrix}. \tag{21}$$

Solving this system of equations allows for the adjustment of bidirectional phase errors.

Unlike traditional correction methods that rely on calibrating various parameters in Eq. (18) using neighborhood information to obtain correction value k, the proposed algorithm adopts a temporal approach to correct phase errors. By employing bidirectional phase projection, sufficient constraint conditions are established, allowing the direct determination of the specific value of k. This algorithm avoids the error accumulation that arises from calibrating numerous parameters, significantly simplifying the correction process. As a result, it offers higher accuracy and stability. It is named the Epipolar Line Phase Correction (ELPC) algorithm.

Point Cloud Fusion

Eq. (20) provides the conversion equation between bidirectional phases. Referring to Fig. 5(b), from Eq. (17), the error variation $\triangle u_v$ after converting the vertical phase v'_p to the horizontal phase u_v can be obtained:

$$\triangle u_v = -\frac{b}{a}\triangle v_p = -\frac{b}{a}k\cos\alpha. \tag{22}$$

Theoretically, in the absence of errors, u_v is equivalent with the horizontal phase u'_p. Therefore, the two can be averaged based on the concept of repetitive projection. In practice, adjusting the system configuration can change the value of b/a. To facilitate the computation, b/a is assumed here to be -1. The final error after phase fusion is:

$$\triangle u_f = (\triangle u_p + \triangle u_v)/2 = \frac{\sqrt{2}k}{2}\sin(\alpha + \frac{\pi}{4}). \tag{23}$$

Visibly, compared to Eq. (17), the error magnitude decreases from k to $\sqrt{2}k/2$. Additionally, phase fusion based on repetitive projection reduces the interference of random noise (Xu et al. 2019). The implementation of this algorithm is straightforward, requiring only the averaging of point clouds reconstructed by bidirectional phase, hence referred to as the Point Cloud Fusion algorithm. Ultimately, this paper further optimizes the bidirectional point clouds generated by ELPC using this algorithm, collectively termed as the Epipolar Line Phase Correction and Point Cloud Fusion (ELPC-PCF) algorithm. The detailed process of ELPC-PCF is shown in Fig. 6. After unwrapping the fringe patterns into absolute phases, the phase errors are calculated and corrected using ELPC. The corrected phases are then converted into the point clouds, and PCF is employed to fuse the two point clouds to obtain the final 3D point cloud result.

Experiment

To futher validate the effectiveness of the proposed method in practical measurement, an FPP-based 3D measurement system is established. The system consists of a computer, a projector (DLP LightCrafter 4500; Texas Instruments, Inc., USA), and a camera (acA800-510um; Basler Vision Technology, Inc., Germany). The resolution of the projector is 912 $\times$ 1140 pixels, and its maximum projection rate is 120 Hz at 8-bit mode. The resolution of the camera is 800 $\times$ 600 pixels, and its maximum frame rate is 393 fps at normal sensor readout mode. The system is 0.7 to 1 meters away from the object to be measured, the angle between the optical axis of the projector and that of the camera is approximately 45°. The system is calibrated by Zhang's method (Zhang 1999) based on four-step phase-shifting method with CGC method (Zhang et al. 2012).

In addition to the proposed method, four existing methods are used to correct these errors: the kernel estimation algorithm (KE) (Xu and Jia 2010), the inverse Fourier transform algorithm (IFT) (Wu et al. 2020), the one-dimensional error model (OEM) (Hu et al. 2023) and the two-dimensional error model (TEM) (Rao and Da 2018). To ensure the objectivity of comparison experiments, all experimental conditions are kept consistent. A total of two comparison experiments are designed. The first experiment measures flat objects. The second experiment measures curved objects. Both experiments include a standard component with regular texture and two conventional objects with irregular texture. Please refer

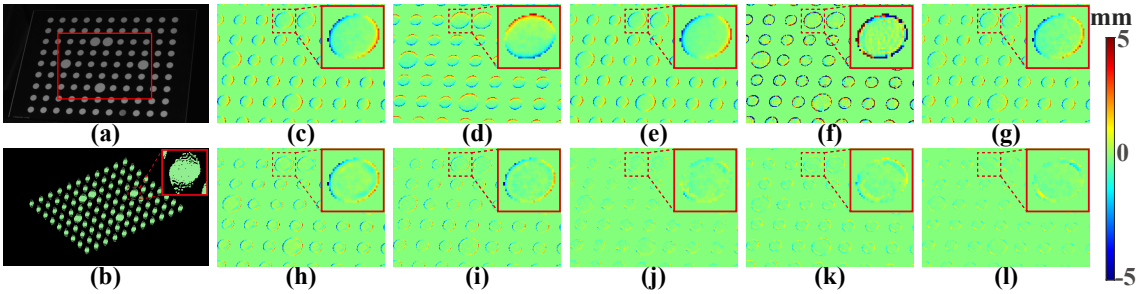

Figure 7: Error distribution of the reconstructed point clouds from the calibration plate. (a) Calibration plate; (b) Point cloud obtained by HPF; (c) Error obtained by HPF; (d) Error obtained by VPF; (e) Error obtained by DHPF; (f) Error obtained by KE; (g) Error obtained by IFT; (h) Error obtained by OEM; (i) Error obtained by TEM; (j) Error obtained by ELPC; (k) Error obtained by PCF; (l) Error obtained by ELPC-PCF.

Method	HFP	VFP	DHFP	KE	IFT	OEM	TEM	ELPC	PCF	ELPC-PCF
MAE	0.645	0.718	0.636	1.312	0.573	0.506	0.397	0.240	0.317	**0.221**
RMSE	1.079	1.160	1.071	10.82	0.974	0.846	0.712	0.377	0.489	**0.348**

Table 1: Errors of the point clouds from the calibration plate.

to **Supplementary Material** for simulation experiments.

Experiment on Flat Objects

The first object measured in this experiment is a calibration plate, a classic standard component that can provide reliable ground truth. As shown in Fig. 7(a), it features severe grayscale transitions at its texture edges, fulfilling the conditions for phase error occurrence. In Fig. 7(b), the reconstructed point cloud also exhibits significant errors. The black regions are prone to the influence of random noise. To focus on addressing the reflectivity mutation and minimize the impact of noise on the reconstruction results, only the white circular regions, which are less affected by intensity noise, are reconstructed. Moreover, texture variations of the calibration plate are relatively simple, with the texture size exceeding the range of the PSF. There is no coupling between adjacent different texture edges. Therefore, its experimental results can intuitively reflect the performance of the algorithm, making it suitable for constructing ablation experiment to verify the contributions of each component of ELPC-PCF.

The surface of the calibration plate is an extremely precise plane, thus enabling the use of plane fitting techniques to obtain its ground truth. The MAE and RMSE between all points in the point cloud and the fitted plane are calculated to assess the measurement accuracy. Figs. 7(c-l) illustrates the error distribution of the region marked by the red rectangle in Fig. 7(a). Figs. 7(c) and (d) represent the errors obtained from horizontal fringe projection (HFP) and vertical fringe projection (VFP), respectively. Notably, the distribution of errors is a trigonometric function of the angle α, which validates the error model in Eq. (17). Given that repetitive projections can suppress random noise, the errors from dual horizontal fringe projections (DHFP) is depicted in Fig. 7(e). The poor correction ability of DHFP indicates that the error is primarily caused by complex textures. Additionally, considering that the results of VFP are worse than those of HFP, the results of VFP and DHFP will not be presented in subsequent experiments. Figs. 7(f-i) presents the errors obtained using the four aforementioned existing methods. It is evident that due to more interference in practical experiments, the error of KE is similar to that of KE in simulated experiments (**Supplementary Material**) but with a larger magnitude. Therefore, this paper concludes that fringe patterns cannot simply and directly use deblurring algorithms designed for conventional patterns. Among this four methods, TEM performs the best. Morover, Figs. 7(j-l) illustrates the results after correction using ELPC, PCF and ELPC-PCF. After ELPC correction, Fig. 7(j) shows almost no noticeable errors, indicating that ELPC effectively addresses the error correction problem for complex textures. The difference between Figs. 7(j) and (l) is minimal, indicating that the proposed ELPC has already effectively corrected phase errors. In ELPC-PCF, the PCF component primarily addresses errors caused by random noise, which are relatively small. Fig. 7(k) indicates that if PCF is used alone, considerable correction effects can also be obtained, which ensures the robustness and versatility of ELPC-PCF. This effect also demonstrates the theory discussed above. Detailed data from each experimental result are listed in Table 1. It is evident that the proposed ELPC-PCF in this paper exhibits exceptional performance, achieving a reduction of up to 65.74% in MAE and 67.75% in RMSE. Compared to TEM, it further reduces the MAE by 27.29% and the RMSE by 33.74%.

The second measured object of this experiment is a card holder, which is only one-sixth the size of the calibration board but features more complex surface textures. As depicted in Fig. 8(a), its surface comprises various complex textures, including line segments, elliptical regions, and circular points, all closely spaced. Following the blurring of captured patterns via the PSF, the adjacent differing textures become coupled, resulting in a more complex error distribu-

tion, as presented in Fig. 8(b). Therefore, its experimental results can afford an enhanced assessment of the actual performance of the proposed algorithm. The surface of the card holder is planar, so its errors can also be determined through plane fitting. Compared to the distinctly visible errors at texture edges in the error distribution produced by other methods, the visualization of ELPC-PCF presented in Fig. 8(h) demonstrates excellent performance, effectively amending the errors. Detailed error metrics are provided in Table 2. ELPC-PCF achieve a reduction of up to 54.03% in MAE and 54.72% in RMSE. It is evident that the proposed ELPC-PCF achieves the best outcomes, even when the object possesses highly complex textures.

The third measured object is a postcard featuring an ole-

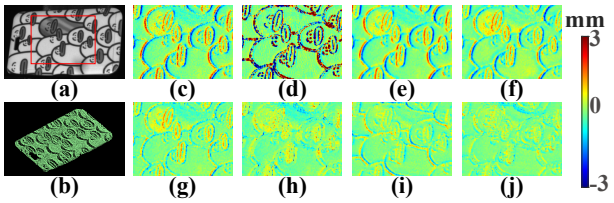

Figure 8: Error distribution of the reconstructed point clouds from the card holder. (a) Card holder; (b) Point cloud obtained by HPF; (c) Error obtained by HPF; (d) Error obtained by KE; (e) Error obtained by IFT; (f) Error obtained by OEM; (g) Error obtained by TEM; (h) Error obtained by ELPC; (i) Error obtained by PCF; (j) Error obtained by ELPC-PCF.

Method	HFP	KE	IFT	OEM	TEM	ELPC	PCF	ELPC-PCF
MAE	0.509	1.742	0.453	0.408	0.332	0.299	0.284	**0.234**
RMSE	0.731	7.525	0.653	0.575	0.469	0.409	0.402	**0.331**

Table 2: Errors of the point clouds from the card holder.

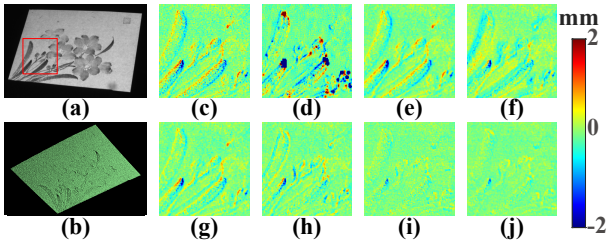

Figure 9: Error distribution of the reconstructed point clouds from the postcard. (a) Postcard; (b) Point cloud obtained by HPF; (c) Error obtained by HPF; (d) Error obtained by KE; (e) Error obtained by IFT; (f) Error obtained by OEM; (g) Error obtained by TEM; (h) Error obtained by ELPC; (i) Error obtained by PCF; (j) Error obtained by ELPC-PCF.

Method	HFP	KE	IFT	OEM	TEM	ELPC	PCF	ELPC-PCF
MAE	0.238	1.132	0.187	0.192	0.169	0.169	0.137	**0.101**
RMSE	0.331	11.00	0.271	0.259	0.241	0.238	0.182	**0.136**

Table 3: Errors of the point clouds from the postcard.

ander illustration. Fig. 9 presents its texture along with the experimental results, with particular attention to the lower-left region, where errors are more pronounced. Its surface has a slight curvature, which provides a challenging scenario to evaluate the robustness of algorithm. Error calculations are performed by fitting the surface to a high-order polynomial function, with detailed results presented in Table 3. Among these method, ELPC-PCF achieved the best performance, reducing MAE by 57.56% and RMSE by 58.91%, demonstrating its stability effectively.

Experiment on Curved Objects

The first object measured in this experiment is a standard sphere with a diameter of 50.4 mm. A black texture is present on the surface of the sphere, as shown in Fig. 10(a), which creates noticeable errors in its point cloud, also illustrated in Fig. 10(b). Similar to the calibration plate, the textures of the sphere do not interfere with each other after being defocused. Therefore, analyzing the error on this sphere can accurately demonstrate the actual error correction performance of ELPC-PCF on curved surfaces. In this experiment, the least squares method is used to achieve spherical fitting of the reconstructed point clouds, thereby calculating the point cloud error for each method, as illustrated in Figs. 10(c-h). Detailed error metrics are tabulated in Table 4. ELPC-PCF achieved the best performance, reducing the MAE by 64.08% and the RMSE by 66.82%. The reconstruction accuracy of the standard sphere can also be judged by the diameter of its fitted sphere. Table 4 shows the diameters of the spheres fitted from the point clouds, denoted as **D**. Based on these data, ELPC-PCF reduces the diameter error by 94.52%. Compared to other methods, ELPC-PCF demonstrates significantly better correction performance. This indicates that even for complex curved objects, it can achieve reliable and efficient measurements.

The second object measured in this experiment is a vase

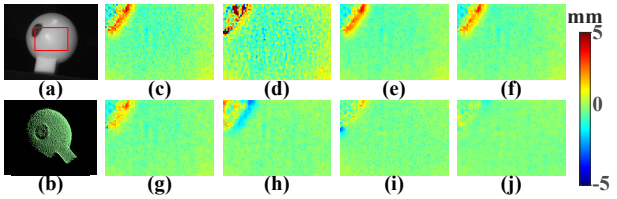

Figure 10: Error distribution of the reconstructed point clouds from the sphere. (a) Sphere; (b) Point cloud obtained by HPF; (c) Error obtained by HPF; (d) Error obtained by KE; (e) Error obtained by IFT; (f) Error obtained by OEM; (g) Error obtained by TEM; (h) Error obtained by ELPC; (i) Error obtained by PCF; (j) Error obtained by ELPC-PCF.

Method	HFP	KE	IFT	OEM	TEM	ELPC	PCF	ELPC-PCF
MAE	0.426	1.076	0.347	0.325	0.281	0.264	0.237	**0.153**
RMSE	0.639	11.46	0.553	0.513	0.438	0.435	0.335	**0.212**
D	47.48	44.88	48.53	48.90	49.35	49.51	48.87	**50.56**

Table 4: Errors of the point clouds from the sphere.

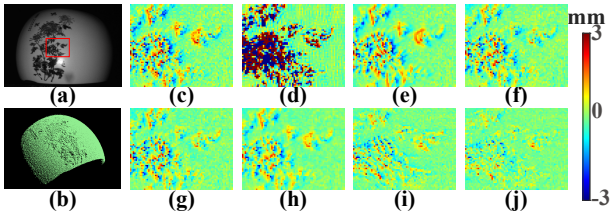

Figure 11: Error distribution of the reconstructed point clouds from the vase. (a) Vase; (b) Point cloud obtained by HPF; (c) Error obtained by HPF; (d) Error obtained by KE; (e) Error obtained by IFT; (f) Error obtained by OEM; (g) Error obtained by TEM; (h) Error obtained by ELPC; (i) Error obtained by PCF; (j) Error obtained by ELPC-PCF..

Method	HFP	KE	IFT	OEM	TEM	ELPC	PCF	ELPC-PCF
MAE	0.473	8.956	0.431	0.394	0.380	0.358	0.331	**0.259**
RMSE	0.702	11.82	0.642	0.588	0.567	0.514	0.480	**0.381**

Table 5: Errors of the point clouds from the vase.

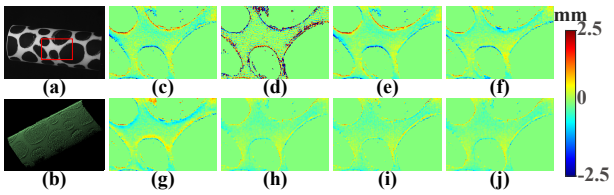

Figure 12: Error distribution of the reconstructed point clouds from the cylinder. (a) Cylinder; (b) Point cloud obtained by HPF; (c) Error obtained by HPF; (d) Error obtained by KE; (e) Error obtained by IFT; (f) Error obtained by OEM; (g) Error obtained by TEM; (h) Error obtained by ELPC; (i) Error obtained by PCF; (j) Error obtained by ELPC-PCF.

Method	HFP	KE	IFT	OEM	TEM	ELPC	PCF	ELPC-PCF
MAE	0.333	2.378	0.302	0.275	0.298	0.251	0.213	**0.184**
RMSE	0.503	50.03	0.465	0.395	0.402	0.376	0.294	**0.260**

Table 6: Errors of the point clouds from the cylinder.

Method	HFP	KE	IFT	OEM	TEM	ELPC	PCF	ELPC-PCF
Time (s)	0.423	8.756	0.367	2.121	0.199	0.106	**0.036**	0.142

Table 7: Time cost of reconstructing 10000 pixels.

with a spherical surface adorned with floral pattern, presenting highly complex textures as illustrated in Fig. 11(a). The depth variations on its surface introduce additional complexity. Moreover, as shown in Fig. 11(a), unlike the previous experiments, the main area of the object has a relatively low grayscale, thus it is more susceptible to interference from random noise. In summary, this experiment underscores a heightened requirement for the performance stability of algorithm. This experiment also employs surface fitting to calculate the point cloud errors for each method, as illustrated in Figs. 11(c-h). Detailed error metrics are tabulated in Table 5. ELPC-PCF achieved the best performance, reducing the MAE by 45.24% and the RMSE by 45.73%. The performance degradation is mainly due to the high proportion of random noise in low reflectivity areas. Compared to the TEM algorithm, the ELPC-PCF algorithm further reduced the MAE by 25.58% and the RMSE by 26.50%.

The third measured object is a paper cylinder with a spotted pattern, as display in Fig. 12, which presents its surface and experimental results. Similar to previous experiments, the point cloud from the black regions is excluded from error calculations to minimize noise interference. The cylinder was crafted using a less standardized process, resulting in a more complex shape than previous measured objects. As in the postcard experiment, its error are calculated by fitting its surface to a high-order polynomial function, with detailed results provided in Table 6. After correction, ELPC-PCF achieved the best performance, reducing MAE by 44.74% and RMSE by 48.31%, which highlights its robustness. These results indicate that the ELPC-PCF algorithm effectively corrects errors caused by complex textures and exhibits good stability.

Additionally, since adding optimization algorithms increases time costs, this section further calculates the time required by each optimization algorithm to reconstruct 10,000 pixels, with detailed data listed in Table 7. Overall, compared to existing methods, ELPC-PCF demonstrates superior real-time performance. Furthermore, its PCF module achieves optimal real-time performance while effectively performing accurate corrections.

Conclusion

To address the phase error issue encountered when the FPP algorithm measures objects with complex textures, a novel approach combining epipolar matching with point cloud fusion (ELPC-PCF) is proposed. Initially, a phase error model at texture edges under camera defocus was analyzed, highlighting the correlation between phase error and both phase and grayscale gradients. Subsequently, the horizontal and vertical fringe patterns were projected to acquire bidirectional phase information. Leveraging this bidirectional phase information, a temporal phase correction algorithm was developed in conjunction with the epipolar matching algorithm and the proposed error model. Different from traditional methods that rely on detailed parameter calibration, this algorithm establishes sufficient constraint conditions, directly determines the correction value, avoids the error accumulation caused by calibrating numerous parameters, and greatly simplifies the correction process. Finally, by calculating and merging the point clouds obtained from the corrected bidirectional phases, the phase error was further minimized. Comparison experiments demonstrate that the ELPC-PCF method can reduce MAE and RMSE by up to 65.74% and 67.75%, respectively. This represents improvements of 27.29% and 33.74% over existing methods, showcasing its enhanced accuracy and stability in reconstructing objects with complex textures.

Acknowledgments

This work is supported by the National Natural Science Foundation of China (Grant No. 62305055) and the Special Project on Basic Research of Frontier Leading Technology of Jiangsu Province of China (Grant No. BK20192004C).

References

Biggs, D. S. C.; and Andrews, M. 1997. Acceleration of iterative image restoration algorithms. *Appl. Opt.*, 36(8): 1766–1775.

Blanchard, C.; and Zhang, S. 2022. Removal of phase artifacts from high-contrast texture for 3D fringe projection system. In *Dimensional Optical Metrology and Inspection for Practical Applications XI*, volume 12098, 19–30. SPIE.

Edgar, M. P.; Gibson, G. M.; and Padgett, M. J. 2019. Principles and prospects for single-pixel imaging. *Nature photonics*, 13(1): 13–20.

Geng, J. 2011. Structured-light 3D surface imaging: a tutorial. *Adv. Opt. Photon.*, 3(2): 128–160.

Hosseini, M. S.; and Plataniotis, K. N. 2019. Convolutional deblurring for natural imaging. *IEEE Transactions on Image Processing*, 29: 250–264.

Hu, C.; Liu, S.; Wu, D.; and Xu, J. 2023. Phase error model and compensation method for reflectivity and distance discontinuities in fringe projection profilometry. *Optics Express*, 31(3): 4405–4422.

Jiang, H.; Li, Y.; Zhao, H.; Li, X.; and Xu, Y. 2021. Parallel single-pixel imaging: A general method for direct–global separation and 3d shape reconstruction under strong global illumination. *International Journal of Computer Vision*, 129: 1060–1086.

Joshi, N.; Szeliski, R.; and Kriegman, D. J. 2008. PSF estimation using sharp edge prediction. In *2008 IEEE Conference on Computer Vision and Pattern Recognition*, 1–8. IEEE.

Khan, D.; Shirazi, M. A.; and Kim, M. Y. 2018. Single shot laser speckle based 3D acquisition system for medical applications. *Optics and Lasers in Engineering*, 105: 43–53.

Kobayashi, T.; Higo, T.; Yamasaki, M.; Kobayashi, K.; and Katayama, A. 2015. Accurate and Practical 3D Measurement for Translucent Objects by Dashed Lines and Complementary Gray Code Projection. In *2015 International Conference on 3D Vision*, 189–197.

Koh, J.; Kim, J.; Yoo, J. H.; Kim, Y.; Kum, D.; and Choi, J. W. 2022. Joint 3d object detection and tracking using spatio-temporal representation of camera image and lidar point clouds. In *Proceedings of the AAAI Conference on Artificial Intelligence*, volume 36, 1210–1218.

Li, J.; and Cheng, X. 2022. Supervoxel-based extraction and classification of pole-like objects from MLS point cloud data. *Optics & Laser Technology*, 146: 107562.

Lyu, N.; Yu, H.; Xu, X.; Bai, L.; Zheng, D.; and Han, J. 2023. Structured light 3-D sensing for scenes with discontinuous reflectivity: error removal based on scene reconstruction and normalization. *Optics Express*, 31(12): 20134–20149.

Lyu, N.; Zheng, D.; Bai, L.; Yu, H.; and Han, J. 2024. Single-pixel imaging-based PSF compensation for large depth-of-field fringe projection profilometry. *Measurement*, 235: 114954.

Ma, Y.; Yin, Y.; Jiang, S.; Li, X.; Huang, F.; and Sun, B. 2021. Single pixel 3D imaging with phase-shifting fringe projection. *Optics and Lasers in Engineering*, 140: 106532.

Nayar, S. K.; Krishnan, G.; Grossberg, M. D.; and Raskar, R. 2006. Fast Separation of Direct and Global Components of a Scene Using High Frequency Illumination. *ACM Trans. Graph.*, 25(3): 935–944.

Qiu, Z.; Zhang, Z.; Zhong, J.; et al. 2020. Comprehensive comparison of single-pixel imaging methods. *Optics and Lasers in Engineering*, 134: 106301.

Quan, C.; Tay, C.; and Chen, L. 2007. A study on carrier-removal techniques in fringe projection profilometry. *Optics & Laser Technology*, 39(6): 1155–1161.

Rao, L.; and Da, F. 2018. Local blur analysis and phase error correction method for fringe projection profilometry systems. *Applied Optics*, 57(15): 4267–4276.

Su, X.; and Zhang, Q. 2010. Dynamic 3-D shape measurement method: A review. *Optics and Lasers in Engineering*, 48(2): 191–204. Fringe Projection Techniques.

Sun, Z.; Duan, M.; Zheng, Y.; Jin, Y.; Fan, X.; and Zheng, J. 2022. Intensity diffusion: a concealed cause of fringe distortion in fringe projection profilometry. *Photon. Res.*, 10(5): 1210–1222.

Wang, Y.; Zhao, H.; Jiang, H.; Li, X.; Li, Y.; and Xu, Y. 2021. Paraxial 3D shape measurement using parallel single-pixel imaging. *Optics Express*, 29(19): 30543–30557.

Wu, R.; Jiang, H.; Zhao, H.; Li, X.; and Guo, Q. 2019. Point spread function measurement for projector based on Fourier single-pixel imaging. In Novak, E.; and Trolinger, J. D., eds., *Applied Optical Metrology III*, volume 11102, 111020T. International Society for Optics and Photonics, SPIE.

Wu, Y.; Cai, X.; Zhu, J.; Yue, H.; and Shao, X. 2020. Analysis and reduction of the phase error caused by the non-impulse system psf in fringe projection profilometry. *Optics and Lasers in Engineering*, 127: 105987.

Wu, Y.; Sun, C.; Zeng, B.; Xie, D.; Liu, S.; and Chen, X. 2016. Geometry-based PSF estimation and deblurring of defocused images with depth information. In *2016 Visual Communications and Image Processing (VCIP)*, 1–4. IEEE.

Xu, L.; and Jia, J. 2010. Two-phase kernel estimation for robust motion deblurring. In *Computer Vision–ECCV 2010: 11th European Conference on Computer Vision, Heraklion, Crete, Greece, September 5-11, 2010, Proceedings, Part I 11*, 157–170. Springer.

Xu, Y.; Zhao, H.; Jiang, H.; and Li, X. 2019. High-accuracy 3D shape measurement of translucent objects by fringe projection profilometry. *Opt. Express*, 27(13): 18421–18434.

Yan, L.; Li, Z.; Liu, H.; Tan, J.; Zhao, S.; and Chen, C. 2017. Detection and classification of pole-like road objects from mobile LiDAR data in motorway environment. *Optics & Laser Technology*, 97: 272–283.

Yao, P.; Chen, Y.; Gai, S.; and Da, F. 2024. Accurate 3D Measurement of Complex Texture Objects by Height Compensation Using a Dual-Projector Structure. *IEEE Transactions on Image Processing*, 33: 3021–3030.

Yue, H.; Dantanarayana, H. G.; Wu, Y.; and Huntley, J. M. 2019. Reduction of systematic errors in structured light metrology at discontinuities in surface reflectivity. *Optics and Lasers in Engineering*, 112: 68–76.

Zhang, F.; Prisacariu, V.; Yang, R.; and Torr, P. H. 2019. GA-Net: Guided Aggregation Net for End-To-End Stereo Matching. In *2019 IEEE/CVF Conference on Computer Vision and Pattern Recognition (CVPR)*, 185–194.

Zhang, Q.; Su, X.; Xiang, L.; and Sun, X. 2012. 3-D shape measurement based on complementary Gray-code light. *Optics and Lasers in Engineering*, 50(4): 574–579.

Zhang, S.; and Yau, S.-T. 2006. High-resolution, real-time 3D absolute coordinate measurement based on a phase-shifting method. *Opt. Express*, 14(7): 2644–2649.

Zhang, Y.; Lau, D.; and Wipf, D. 2021. Sparse Multi-Path Corrections in Fringe Projection Profilometry. In *2021 IEEE/CVF Conference on Computer Vision and Pattern Recognition (CVPR)*, 13339–13348.

Zhang, Y.; Lau, D.; and Yu, Y. 2019. Causes and Corrections for Bimodal Multi-Path Scanning With Structured Light. In *2019 IEEE/CVF Conference on Computer Vision and Pattern Recognition (CVPR)*, 4426–4434.

Zhang, Z. 1999. Flexible camera calibration by viewing a plane from unknown orientations. In *Proceedings of the seventh ieee international conference on computer vision*, volume 1, 666–673. Ieee.

Zhang, Z.; Wang, X.; Zheng, G.; and Zhong, J. 2017. Fast Fourier single-pixel imaging via binary illumination. *Scientific reports*, 7(1): 12029.

Zuo, C.; Feng, S.; Huang, L.; Tao, T.; Yin, W.; and Chen, Q. 2018. Phase shifting algorithms for fringe projection profilometry: A review. *Optics and Lasers in Engineering*, 109: 23–59.